Mattos, B. D.; Tardy, B. L.; Greca, L. G.; Kämäräinen, T.; Xiang, W.; Cusola, O.; Magalhães, W. L.E.; Rojas, O. J.

Nanofibrillar networks enable universal assembly of superstructured particle constructs

Published in:
Science Advances

DOI:
10.1126/sciadv.aaz7328

Published: 01/05/2020

Document Version
Publisher's PDF, also known as Version of record

MATERIALS SCIENCE

Nanofibrillar networks enable universal assembly of superstructured particle constructs

B. D. Mattos[1], B. L. Tardy[1]*, L. G. Greca[1], T. Kämäräinen[1], W. Xiang[1], O. Cusola[2], W. L. E. Magalhães[3], O. J. Rojas[1,4,5]*

Superstructured colloidal materials exploit the synergies between components to develop new or enhanced functions. Cohesion is a primary requirement for scaling up these assemblies into bulk materials, and it has only been fulfilled in case-specific bases. Here, we demonstrate that the topology of nanonetworks formed from cellulose nanofibrils (CNFs) enables robust superstructuring with virtually any particle. An intermixed network of fibrils with particles increases the toughness of the assemblies by up to three orders of magnitude compared, for instance, to sintering. Supramolecular cohesion is transferred from the fibrils to the constructs following a power law, with a constant decay factor for particle sizes from 230 nm to 40 μm. Our findings are applicable to other nanofiber dimensions via a rationalization of the morphological aspects of both particles and nanofibers. CNF-based cohesion will move developments of functional colloids from laboratory-scale toward their implementation in large-scale nanomanufacturing of bulk materials.

INTRODUCTION

Presently, up to the microscale, particle assemblies can bear a high level of modularity (*1*–*4*), with an extensive set of new and enhanced functionalities arising from the surface chemistry and the morphology of the building blocks as well as their hierarchical organization (*5*, *6*). These assemblies have shown outstanding performance in electrochemistry (*7*), catalysis (*8*), sensing (*9*), photonics (*10*), and controlled delivery platforms (*11*, *12*). However, the scaling up of colloidal assemblies into cohesive bulk materials is still a standing challenge within nanomanufacture. Although the engineering of supramolecular cohesion of polymers has revolutionized modern-day manufacturing (*13*), this engineering of macroscaled cohesion in particulate networks and lattices still faces particle-dependent limitations. Sintering (*12*) and secondary interactions (*14*) are often used for binding networks of inorganic and polymeric particles. Several restrictions, however, arise depending on the building blocks, for instance, for biological or surface-active particles. These particles cannot be processed at high temperatures due to their sensitivity, nor can they be incorporated into a polymer melt as it would limit access to their surface. In addition, networks can be formed spontaneously at room temperature by oriented attachment, with restricted applications to small particles with high interfacial energy and Brownian motion that promote their assembly (*15*, *16*). The compositional dependence on the formation process is a major issue for scale-up efforts, and it expressively limits developments of new nanomanufactured materials. Therefore, the development of macrofabrication processes—under mild conditions and suitable for a wide range of particles—is paramount.

Here, we explore the complex topology of highly interconnected fibrillar networks formed by supramolecularly cohesive fibers (*17*–*20*) to achieve particle independency within macrofabrication. We used cellulose nanofibrils (CNFs)—biocolloids derived from plants or bacteria—as they are the best candidates for this purpose due to their high strength [E_A up to 100 GPa (*21*)], branched morphology, and high flexibility that yield an interconnected nanonetwork with entangled contact points (*22*). These features have been exploited to achieve upper boundaries in terms of mechanical strength in foams, filaments, and films only formed from CNFs (*23*). Furthermore, so far, CNF-based matrices were infused with particles of varying size, morphology, and surface chemistry to produce, for instance, high-performance, thermally insulating, and fire-retardant foams (*20*), as well as magnetic (*24*) and conductive (*25*, *26*) aerogels and nanopapers.

CNFs have been shown to enable the structuring of particles [e.g., zeolites (*27*), metal-organic frameworks (*28*), and TiO_2 (*29*)], and here, we demonstrate the universal application of CNF to induce cohesion in particle constructs even if incorporated at extremely low fractions. We show that the ability of CNF to form a topologically complex network with high supramolecular cohesion is linked to the high aspect ratio of the fibrils (nanometers wide and up to several micrometers long; Fig. 1A) (*30*). The flexibility of the fibrils, with the smallest rigid unit sizing at approximately 150 nm long (*31*), is demonstrated to play a key role enabling a conformation-dependent response to capillary stresses upon drying, where the fibrils experience proportionally high forces (*32*, *33*). These forces link the secondary supramolecular interactions between fibrils, which are similar to those present within the crystalline domains of nanocelluloses, resulting in assemblies with cohesion mechanisms mirroring those observed at the molecular level (*34*). We investigate CNF-induced cohesion in particulate composites using a broad variety of spherical, millimetric materials subjected to evaporation-induced self-assembly (EISA) of aqueous suspensions onto superhydrophobic surfaces (*35*–*38*). Specifically, we establish the compositional limits for CNF-induced cohesion, from which we introduce scaling factors to determine the mechanical strength of the constructs as a function of the size, composition, and surface

[1]Department of Bioproducts and Biosystems, School of Chemical Engineering, Aalto University, FI-00076 Espoo, Finland. [2]Universitat Politècnica de Catalunya, Escola Superior d'Enginyeries Industrial, Aeroespacial i Audiovisual de Terrassa, 08222 Terrassa, Spain. [3]Embrapa Florestas, Estrada da Ribeira km 111, 83411-000 Colombo, Paraná, Brazil. [4]Department of Applied Physics, School of Science, Aalto University, FI-00076 Espoo, Finland. [5]Departments of Chemical and Biological Engineering, Chemistry and Wood Science, University of British Columbia, 2360 East Mall, Vancouver, BC, Canada.
*Corresponding author. Email: orlando.rojas@aalto.fi (O.J.R.); blaise.tardy@aalto.fi (B.L.T.)

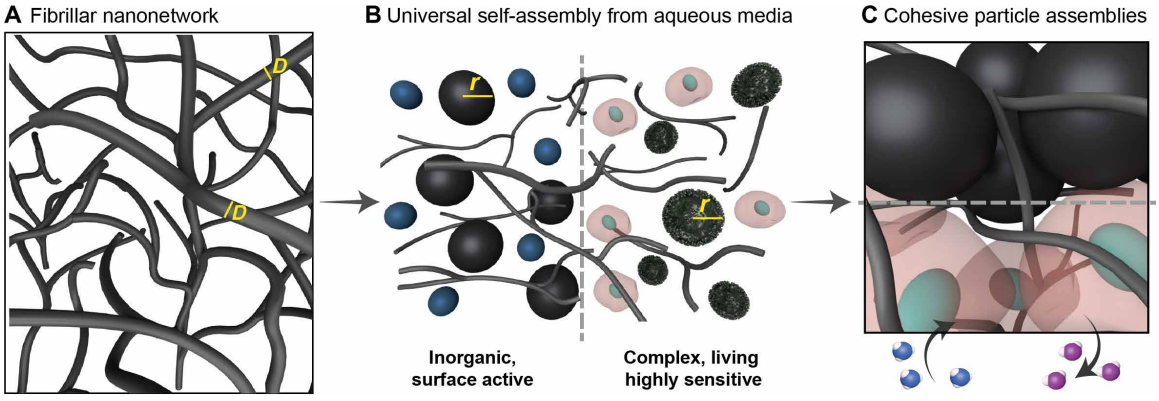

Fig. 1. CNFs are robust, flexible, and nanoscaled plant-based building blocks. (**A**) The fibrils form a highly entangled and networked 3D structure with multiple, entangled contact points. (**B**) The special topology of the CNF nanonetwork is loose in suspension, thus allowing the co-dispersion of a broad variety of particles within the interconnected nanofibrillar structure. (**C**) During self-assembly from aqueous media, a dried interlocked network of particles and fibrils is formed. Extremely high cohesion is introduced from minimal fibril-particle interactions, which is essential to maintain the surface access to the primary particles and their functionalities.

chemistry of the primary components (Fig. 1B). The cohesion introduced by CNF is evaluated as a function of interfibril, fibril-particle, and interparticle interactions relative to the respective surface areas of the components involved. We identified that the CNF-driven cohesion arises mostly from interfibril interactions, thus allowing a successful macrofabrication of particles with a range of characteristic geometries and with diverse surface energy, charge, and sizes. Our analytical framework and numerical findings point to the formidable potential of CNFs to act as an extremely efficient cohesion-inducing additive while maintaining the access to the surface of the primary particle as well as their functionalities (Fig. 1C). In addition, the provided scaling laws are extended to account for the flexibility and dimensionality of other nanocelluloses to rationalize and expand the opportunities of developing bulk particle constructs using a universal formation process.

RESULTS

Effect of particle size in the assembly of CNF-particle networks

Particle-based composites were formed from CNFs obtained by mechanically fibrillated wood fibers (WFs), with minimal electrostatic charges (*39*), and SiO_2 particles that were chosen for their high synthetic tunability as far as size and surface chemistry. Aqueous suspensions incorporating CNF and SiO_2 particles (from 20 nm to 40 μm) were assembled into spherical supraparticles (SPs) via EISA onto a superhydrophobic substrate (fig. S1A).

SPs with an identical diameter (ca. 1.5 mm) can be obtained by adjusting the solid fraction of the suspensions and the casting volume (fig. S1, B to F). Figure 2 (A to E) illustrates the architectural differences in the networks formed in the CNF-particle constructs as a function of particle size. Within the same CNF fraction, the microstructures of the materials are governed by the relationship between the relative specific surface areas (SSA) for particles and CNF (SSA ratio; details described in fig. S2). Still within a given CNF fraction, the SSA ratio has a negative relation with the particle size, i.e., the higher the SSA ratio, the smaller the particles. The CNF networks formed across the SPs (Fig. 2, A to E) were analyzed by selectively dissolving the SiO_2 nano- and microparticles (Fig. 2F). Structures ranging from a three-dimensional (3D) continuous network (with length scales of approximately 50 nm) to micrometer-scaled cellular architectures were observed depending on the size of the SiO_2 particles (20 nm, 230 nm, and 40 μm) (Fig. 2, G to I). The CNFs assemble into sheets on the larger microparticles (SSA ratio equal to 0.003), subsequently forming the walls of honeycomb-like unit cells with a curved center (Fig. 2I). Upon uniaxial compression, the highly interconnected, 40-μm–based, particle-free CNF network behaves as a conventional cellular foam (fig. S3). The initial ascending zone of the compression profile shows the unit cells elastically bending, followed by a buckling plateau that results from plastic deformation and the densification regime taking place when the opposing cell walls continue to buckle until they eventually touch (*19*). In the 40-μm–based SPs, however, the balance between interfibril and CNF particle is not optimal because of the relative low surface area of the particles that prevents the formation of a 3D network to distribute more efficiently the mechanical stresses.

The isolation of the fibrils from the 20-nm–based SPs yielded a dense and continuous 3D network (Fig. 2G). From the relatively high SSA ratio (~7.5) of the smallest particle size (20 nm), we can expect that several particles interact with a single CNF, especially at the latter stages of EISA. The dimensional similarity of the fibrils and the 20-nm SiO_2 promotes an intermediate behavior where the assembly did not favor high interfibril entangled but only several well-spaced, partial connection points. The force-strain profiles for the 20-nm–based CNF network resemble the mechanical behavior of aerogels (fig. S3), where there is a continuous densification of a porous network that continues over large strains (*19*, *40*). SPs formed from particles with a diameter of 230 nm, with SSA ratio closer to 1, displayed the best compromise in terms of composition and mechanical strength of the final CNF-particle construct (Fig. 3). Their intensified fibril-particle connectivity is further verified by scanning electron microscopy (SEM) images (Fig. 2H), where a clear collapsing of the CNF network occurred upon the dissolution of the SiO_2 particles. This is due to some interactions being uniquely of the fibril-particle type, leaving end sections of the fibrils disconnected from any network after the removal of the particle component (Fig. 2H, inset). Furthermore, the typical compressive profiles obtained for the 230-nm–based CNF network showed the weakest mechanical performance (fig. S3). An optimized interfibril and fibril-particle coupled binding is therefore essential to achieve robust materials from very low CNF fractions.

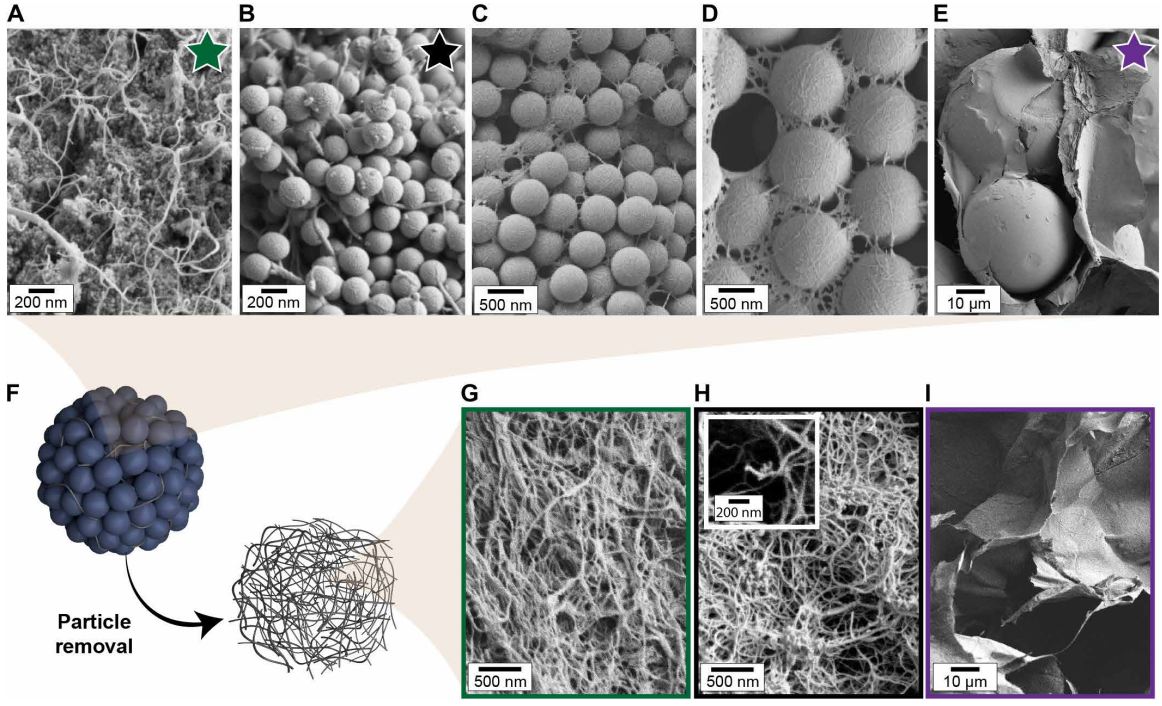

Fig. 2. Formation of robust, dried particle assemblies induced by CNF for a wide range of particle sizes. (**A**) CNFs with colloidal particles (20 nm), (**B**) 230 nm, (**C**) 500 nm, (**D**), 1.15 μm and (**E**) 40 μm in diameter. The micrographs show a change from fully formed 3D network of disconnected CNFs (A) to 2D entangled networks (E) as the particle size is increased. (**F**) Isolation of the CNF networks for the evaluation of their characteristics. (**G** to **I**) SEM images of the isolated CNF network formed from (G) 20-nm, (H) 230-nm, and (I) 40-μm SiO_2 particles, showing networks ranging from continuous nanoscaled to microscaled cellular architectures.

Scaling behavior of the CNF-induced mechanical cohesion

Compared to traditional processes for inducing cohesion in SiO_2 SPs (for example, sintering), those formed with cellular or continuous CNF networks for particle binding showed a remarkably better mechanical performance (Fig. 3 and fig. S4, A and B). The toughness is higher for all particle sizes (fig. S4, C and D). For instance, the toughness increased by 2000% for CNF-bound SPs built from 230-nm SiO_2, compared with their sintered counterpart (Fig. 3A). This improvement is a result of an extended elastic-plastic regime (I) with two additional toughening mechanisms, namely, the cracking hindrance plateau (II) and the compaction regime (III), both of which are absent in typical particle aggregates (*41*) due to their catastrophic failure at the end of regime (I).

We used the static force at the threshold between regimes (I) and (II)—the yield point (Fig. 3A)—to compare the cohesion of the variety of SPs prepared. The force at this point corresponds to the maximum loading, where the entangled, nonconnected fibrils are fully stretched, before cracking and slippage take place. Therefore, the yield point numerically describes the total contribution from the fibrils to the cohesion of the construct, which is the interfibril and particle-fibril interactions, with the assumption that the interparticle interactions are relatively negligible. The yield point was normalized by the volume of the SP, resulting in a volume-specific strength (N mm^{-3}) that enabled comparison between SPs of different sizes (fig. S5).

Using a variety of SPs, we described a numerical correlation between the relative surface area between particles and CNFs (SSA ratio; fig. S2) with the cohesion of the formed network (Fig. 3, B and C). For a given particle size, the SSA ratio decreases as the CNF fraction increases. The CNF fraction has a positive effect in the cohesion of the SP, regardless of the SiO_2 particle size (fig. S4). For all particle sizes, the yield point under compression of the SPs scales universally according to a decaying power law [$f_{(x)} = a \cdot x^k$] with the CNF fraction. The proportionality constant a from the power law fit follows a linear log-log relation for a wide range of particle sizes (Fig. 3D), from 230 nm to 40 μm. Within this size range, the scaling of the SPs' cohesion as a function of the SSA ratio is described by the decay factor k that is constant ($k = -1.4$). The cohesion of the SPs made with colloidal SiO_2 particles (20 nm), however, decays by a factor of approximately 0.6. To distinguish the cohesion of the network arising from interfibril interactions from those arising from the fibril-particle interactions, CNF-based SPs with hydrophobic and cationic SiO_2 particles (further referred to as $SiCH_3$ and $SiNH_3^+$) were prepared. First, the hierarchical architecture of the SPs built from hydrophobic and cationic SiO_2 particles (230 nm) differs greatly from the continuous 3D particle CNF network that is observed in SPs built from unmodified particles of the same size (Fig. 2B). A near-zero surface potential on the $SiCH_3$ particles led to high interparticle attraction in the suspension—driven by hydrophobic interactions—and, thus, led to sheet-like CNF networks forming around large hydrophobic particle aggregates (fig. S6, A to C), which were observed for the 40-μm SiO_2–based SPs (Fig. 2E and fig. S6, D and E). In the case of SPs built with $SiNH_3^+$, the positively charged particles are attracted very strongly by the slightly negative cellulosic surfaces via ionic interactions, thus inducing the rapid formation of suspended aggregates with CNF that are sparsely dispersed around the network after its consolidation into a dried material (fig. S6, F to H).

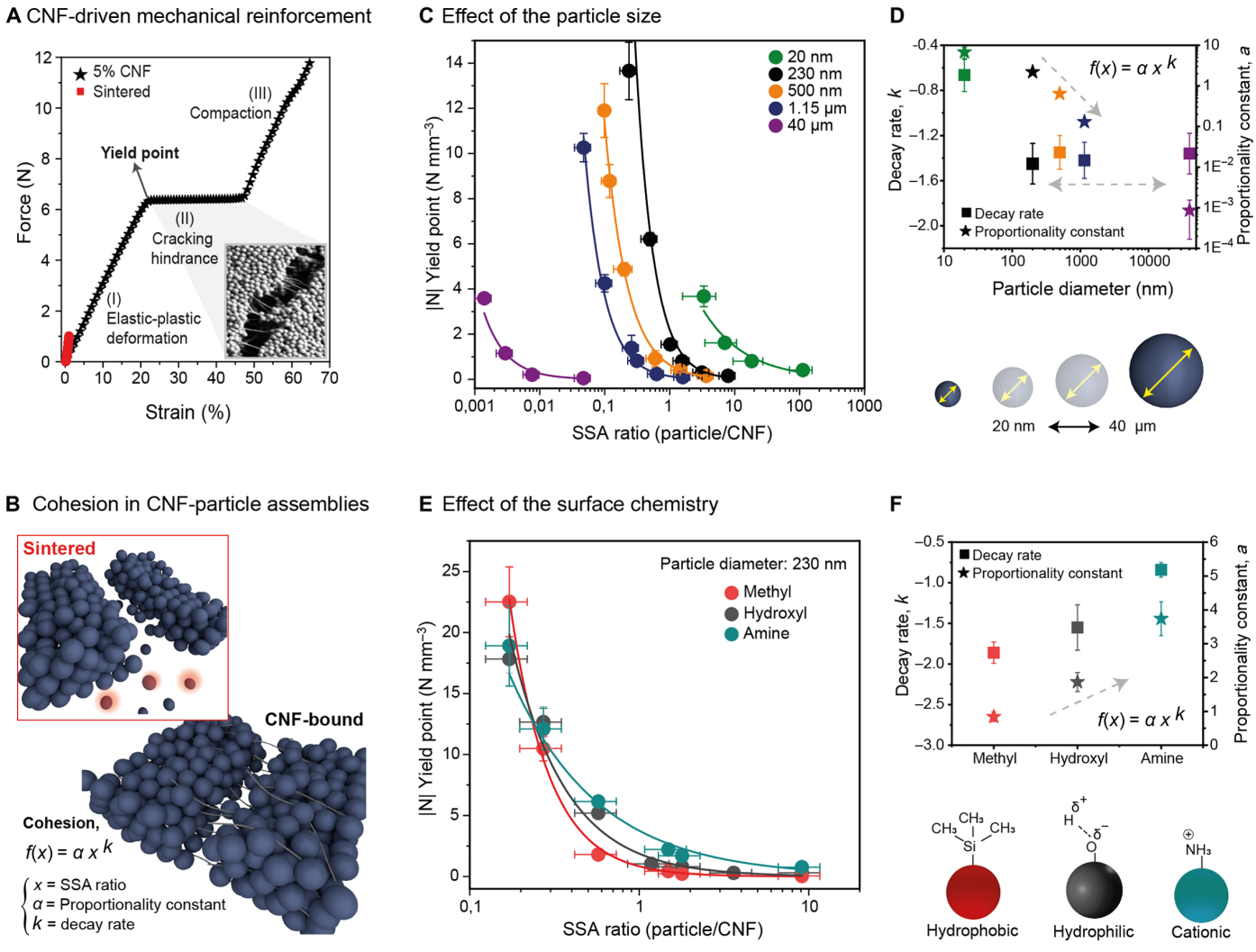

Fig. 3. Development of cohesion by using CNFs in SP assemblies and scaling as a function of the particle size and the surface chemistry. (**A**) Typical uniaxial compression force-strain profile of 230-nm SiO_2-based SPs prepared in the presence of CNF (5% loading) and for SiO_2 SPs sintered at 600°C for 2 hours in the absence of CNF. The panel includes the critical points that are used for comparison and the different regimes (I to III) that define the reinforcement effect of CNF in the system. The inset SEM image shows the morphology of the cracking area of a CNF-bound SiO_2 (230 nm) SP. (**B**) Schematic representation of the cracking hindrance effect and cohesion brought by the CNF and comparison with their sintered counterparts. (**C**) Scaling of the yield point of the SP as a function of the particle size and CNF fraction, here approached as relative surface area (SSA ratio). (**D**) Proportionality constant (*a*) and decay rate (*k*) obtained from the power law fittings. (**E**) Scaling of the yield point of the SP as a function of the surface chemistry and CNF fraction, here approached as relative surface area (SSA ratio). (**F**) Proportionality constant (*a*) and decay rate (*k*) obtained from the power law fittings.

Notably, the strength of SPs prepared with $SiCH_3$ and $SiNH_3^+$ was greatly improved when increasing the CNF fraction (Fig. 3E). A high and similar toughness is observed for all SPs prepared, regardless of the distinct surface chemistries of the SiO_2 particles (fig. S7). However, the scaling for CNF-induced cohesion of the networks has strong dependence on the surface chemistry of the primary building blocks. The cohesion displayed by the $SiCH_3$-based SPs decays sharper ($k = -1.85$) as a function of the SSA ratio compared to the unmodified SiO_2 ($k = -1.4$). Furthermore, the cohesion of SPs built from $SiNH_3^+$ decays at a remarkably lower rate ($k = -0.84$) (Fig. 3F).

Universal CNF-induced cohesion in particle assemblies

We further evaluate the high adhesion provided by CNF with particles with a broad spectrum of dimension, geometry, and composition (Fig. 4, A and B, and fig. S8). Figure 4B demonstrates the potential for creating bulk materials from particles using CNFs to induce cohesion. The scaling law developed here for the yield point as a function of the SSA ratio for spherical SiO_2 particles extends to other spherical particles: Fe_3O_4 (80 nm), TiO_2 (30 nm), lignin (330 nm), and polystyrene (400 nm). In all cases, the yield point of the assemblies scaled similarly to observations for the SiO_2 particles. More complex particles, including those of biological origin (pollen and yeast) and nonspherical ones (clay platelets and nanotubes), do not follow the same scaling (Fig. 4, A and C). Notably, biological materials form very cohesive particle networks, even with a relatively low SSA ratio (larger particles). This indicates strong interactions with nanocelluloses as well as strong interparticle affinity, which are factors that are not considered in our scaling law. The higher-level

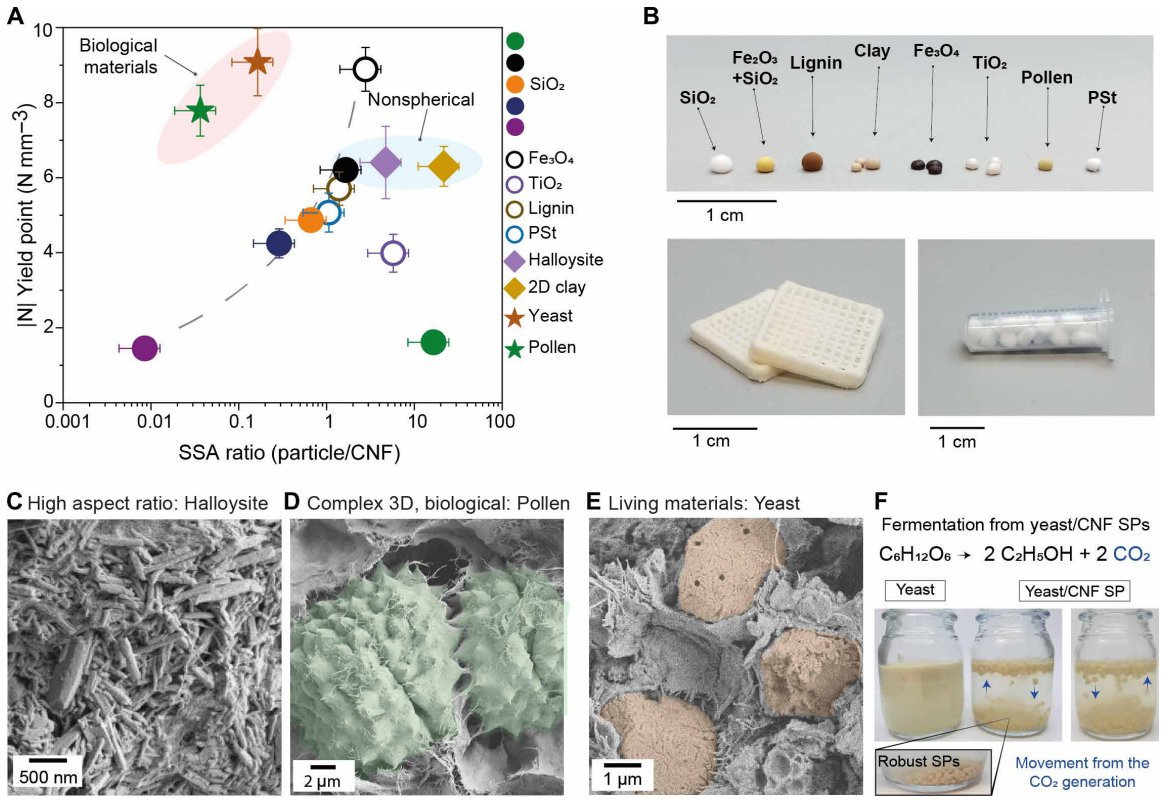

Fig. 4. Assessment of the cohesion capacity of CNFs with particles varying in both chemical complexity and morphology. Particles of different shapes, origins, packing ability, and aspect ratio are used in the synthesis of robust SPs. (**A**) Scaling of the SPs' robustness as a function of their respective SSA ratio. (**B**) Photograph of the obtained materials and a 3D printed object (direct ink writing) to illustrate the prospects for scalability of the CNF-particle materials (230-nm SiO_2 and CNF). (**C** to **E**) SEM images of few examples of biological materials and high aspect ratio particles that are superstructured with CNFs. In (D) and (E), the particles were artificially colorized. (**F**) Demonstration of the preserved functionalities (fermentation process) of the living yeast particles after superstructuring with CNFs from aqueous suspensions. Photo credits: Bruno D. Mattos (Aalto University).

hierarchy of the particles may also, for instance, induce anchoring points for the CNFs to entangle and form stronger networks (Fig. 4, D and E). Superstructuring from aqueous suspensions of CNF preserved the metabolic functions of the living yeast particles, in which CO_2 and ethanol are produced from sugars (sucrose and glucose) and further released from the SPs at a rate that depends on the availability of the nutrients (Fig. 4F and movies S1 and S2). We attribute the high robustness observed for the halloysite (Fig. 4B) and 2D clay to their intensified surface interactions coming from tighter packing compared to spherical particles. For instance, for the same SSA ratio, the spherical particles have yield points at least fivefold smaller when compared to the 2D clay platelets (Fig. 4A).

Morphological features of CNF inducing cohesion and prediction prospects

To gain insight into the fibril networking and its potential to introduce cohesion in particulated constructs, we numerically evaluated the morphology and flexural properties of the CNFs, as well as the CNF-particle formulation aspects. The interactions at the fibril-particle interface could be assessed considering the conformability of CNF around the particles (Fig. 5A). We assumed a linear chain of rigid elements' morphology for the fibrils by varying both the dimension of the rigid elements (L) and the maximum angle of rotation (θ) (Fig. 5B). The surface corresponding to the transition between the fibrils that can conform around the particles (blue projection) or conforming a maximum of two segments (red projection) is shown in Fig. 5 (A and C1 to C5) as a function of θ, L, and D (the diameter of the SiO_2 particles). The dashed white lines represent given SiO_2 diameters used in this study. When extracting the corresponding (θ, L) planes (Fig. 5, C1 to C5), almost completely amorphous fibers (very short L and extremely high θ) would be required to conform around the 20-nm SiO_2, whereas even extremely crystalline fibers (with $L > 1$ µm) could conform around the micrometer-sized SiO_2. Considering that the highest cohesion was observed in the SPs built from 230-nm SiO_2 particles, high conformational flexibility does not translate into high cohesion. The conformability map for 230-nm particle diameter shows that nonconformal, rigid CNF configurations most likely prevail (Fig. 5C2). Compared to other nanoscaled fibers (*42*, *43*), the conformability of CNFs around complex topographies enables a wide variety of robust topologies (Figs. 2 and 3).

The aspects related to the spatial distribution of the fibrils among the particles were analyzed in the dispersed state because of the inherent presence of voids in the dry state. The results were then correlated with the yield point of the dried SPs. The highest yield point is attained for SPs built from 230-nm SiO_2 with 15 weight % (wt %) of CNF added (Figs. 3 and 5A). At this composition, the fibrils and particles are close to equal number ($n_{CNF}/n_{SiO2} \approx 3.7$; Fig. 5B), displaying around one to two fibrils surrounding a single SiO_2 particle in suspension. Such a ratio of the components is specific to the morphology of CNF used here, for which 230 nm is optimal

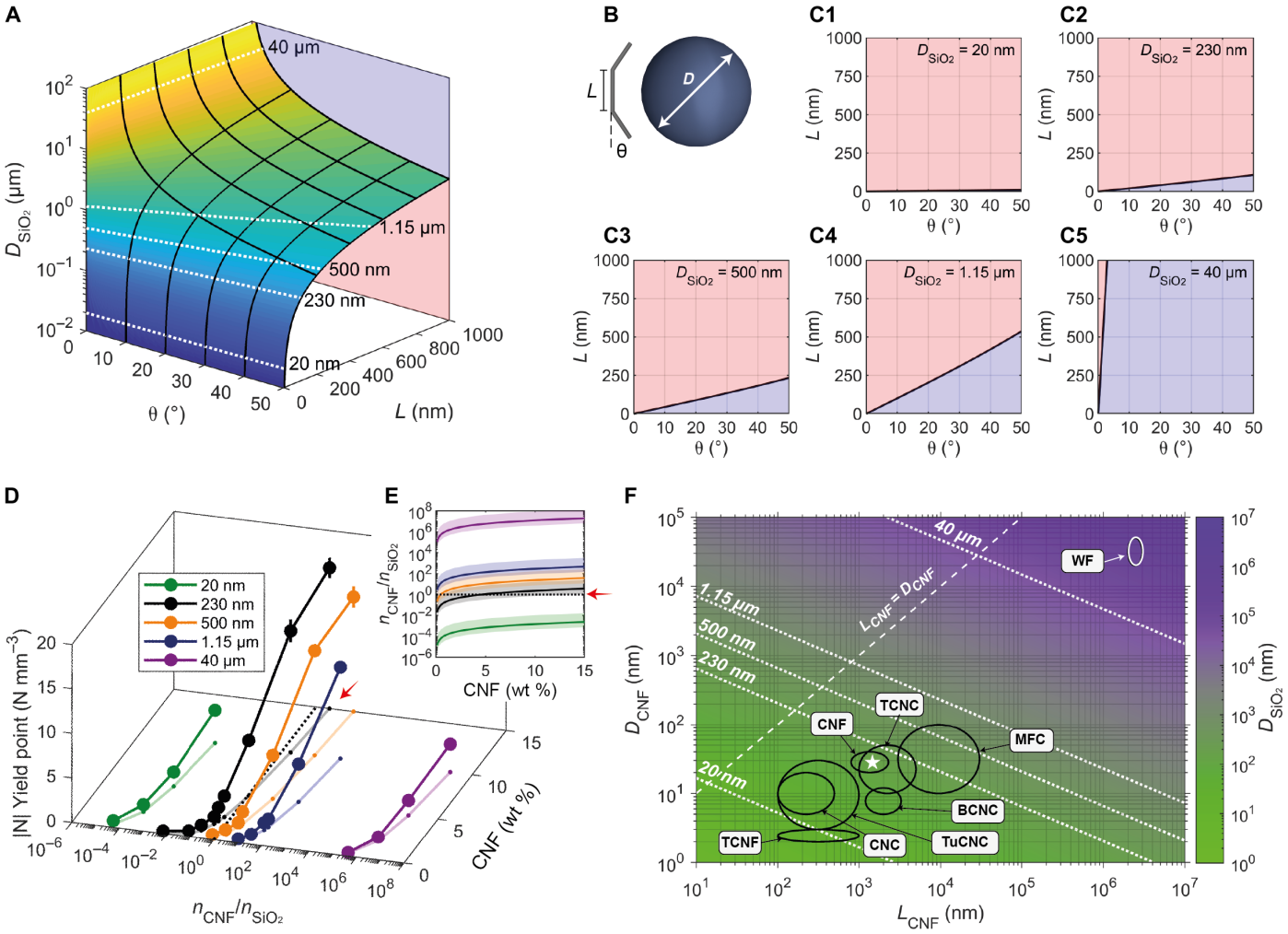

Fig. 5. Physical interpretation of CNF morphological attributes inducing cohesion in particulated networks. (**A**) Conformability of the CNFs modeled as a linear chain of rigid segments of length *L* and maximum deformation angle θ between subsequent segments as demonstrated in (**B**). (**C1** to **C5**) Conformability threshold of CNF around SiO_2 particles of given sizes. Within the area shown in red, only two segments touch the particle, whereas in the blue (bottom) area, the CNF fully conforms around a SiO_2 particle of given diameter. (**D**) Mechanical performance of the SPs as a function of the ratio between the CNFs and the SiO_2 particles (n_{CNF}/n_{SiO2}) and CNF fraction (%). (**E**) CNF-to-SiO_2 number density fraction (n_{CNF}/n_{SiO2}) as a function of CNF fraction (%) in the SPs. The red arrows in (D) and (E) show n_{CNF}/n_{SiO2} of D_{SiO2} = 230 nm approaching 1 at CNF = 15%. (**F**) Probe of the parameter space for optimized compressive strength based on the experimental results shown in (D), in which the highest mechanical strength is found when $n_{CNF}/n_{SiO2} \approx 3.7$ at 15% CNF. The likely values for the length (*L*) and diameter (*D*) of CNF are shown to attain $n_{CNF}/n_{SiO2} \approx 3.7$ at 15% CNF at given SiO_2 diameter. Other grades of nanocelluloses are marked in (F), suggesting the particle size range where they could induce cohesion. CNF, cellulose nanofibrils (*39*); CNC, cellulose nanocrystal (*57*); TCNF, TEMPO-oxidized CNFs; TCNC, TEMPO-oxidized cellulose nanocrystals; BCNC, bacterial nanocellulose from coconut pulp (*58*); TuCNC, cellulose nanocrystals from tunicate (*59*); MFC, microfibrillated cellulose; WF, wood fibers (*22*).

($L = 1.4 \pm 0.8$ µm and $D = 28 \pm 12$ nm). Although the free volume of a low-concentrated 230-nm SiO_2 suspension (5 wt %) can accommodate multiple fibrils side by side (fig. S9B), the suspension is very sparsely populated by fibrils over most of the compositions used here (fig. S9C2). In the corresponding initial suspension (230 nm at 5 wt %), the particles are spaced on average $\langle\delta\rangle \approx 120$ nm apart (fig. S9A), which, parallel with the nonconformal aspects, implies that a single CNF would extend lengthwise over approximately four particles. The network structure is hence highly intermixed with SiO_2 particles, unable to form sheet-like CNF constructs. Particles with 20 nm and 40 µm diameters denote boundary cases relative to the physical constrains of the CNFs, both displaying the lowest mechanical performance among the SPs prepared. There is no case where the CNF can conform around 20-nm particles due to their very small radius of curvature (Fig. 5C1). In addition, $\langle\delta\rangle$ values are too small (<10 nm) to allow the fibrils to locate between them (fig. S9B), while the particles are far too numerous to create an intermixed structure with CNFs (fig. S9C1). This formulation-related aspect favored the formation of extensive particle-rich regions embedded in the surrounding irregular network of CNFs (Fig. 2A). An opposite situation took place for the systems comprising 40-µm particles, where the interstitial space is several orders of magnitude higher than the diameter fibrils, thus resulting in minimal conformability (Fig. 5C5) and allocation (fig. S9, A and B) restrictions.

On the basis of our experimental data and numerical analysis, we can infer that to maximize CNF-based cohesion, one must preserve

near one-to-one number ratio between the CNFs and the particles to create an intermixed particle-fibril network. To obtain an equivalent network but in a broader dimensional space of interest, we propose an equivalent fibrillar morphology, at a given flexibility, that is required to form a similar network. The morphology parameters L and D of the fibrillar adhesive, yielding a similar network, are plotted in Fig. 5F (and fig. S10) as a function of the particle diameter (D) that is displayed as an isosurface map, where constant conditions of $n_{CNF}/n_{SiO2} = 1$ and 15 wt % of CNF are assumed. Several fibrillar morphologies fulfill these conditions within a given particle size; however, and more interestingly, on the basis of these conditions, one can estimate optimal formulation conditions to induce cohesion in other particle sizes. For instance, it is reasonable to infer that TEMPO-oxidized CNF would promote cohesion in constructs built from particles with a diameter below 100 nm. Thus, WFs would already maximize the cohesion in micro- or millimeter particle aggregates. We experimentally validated our analytical model by preparing SPs containing WFs and 40-μm SiO_2 particles, as well as SPs containing smaller SiO_2 particles (230 nm) superstructured with CNFs obtained at different degrees of mechanical deconstruction [microfluidization at higher levels of severity or number of passes yields fibrils of reduced dimensions (*44*)] as well as TEMPO-oxidized CNF (fig. S11). Although not in the optimum range for near one-to-one particle-fiber network (Fig. 5F), a considerable high cohesion was introduced for 40-μm–based SPs formed from WFs. The values for the yield point of CNF- and WF-bound 40-μm SPs are in the same order of magnitude (0.68 and 0.45 N mm^{-3}), which implies a cohesion limit imposed by the relative dimensions of the fibrils compared to the particles. This cohesion threshold, for a given fibril fraction, is also observed when combining 230-nm SiO_2 particles with CNFs of decreased size. Mildly defibrillated CNF (large CNFs obtained after one and three passes) resulted in a limited cohesion in 230-nm–based SPs; however, as shown in this contribution, highly defibrillated CNF (after six passes) endowed a maximum cohesion in the respective construct. No further improvement was observed for the smaller fibrils (9 and 12 passes and TEMPO-CNF; fig. S11A).

DISCUSSION

SP formation and development of cohesion

The particle-CNF mixtures used here formed loose networks in suspension (figs. S12 and S13) but extremely cohesive networks in the dried state, as shown in Fig. 3. The lack of interactions between the two components before gelation is also suggested from rheology tests conducted with particle-CNF mixtures at given concentrations representing different EISA stages (CNF, 0.75 to 3 wt %; particles, 5 to 20 wt %). This is supported by a sustained elastic behavior with increased concentration, with G' > G" and thus tangent loss < 1 (fig. S13, D to F). In addition, the slope of the viscosity profiles did not change, displaying shear thinning until the later stages of the assembly (fig. S13, A to C). This implies that there was no disruption of the entanglements between the fibrils until the late stage of assembly. At the earliest EISA stages, fibril-particle and interfibril connections are relatively weak due to the highly ordered layers of bound water that form on the surface of cellulose (*45*–*48*). With the removal of free water, and sequentially bound water, taking place at the later EISA stages, high capillary forces bring the fibrils together at distances below 2 nm, triggering short-ranged forces (multiple H-bonding and van der Waals interactions at distances <0.5 nm), leading to the formation of a tight and highly cohesive system (*33*, *49*, *50*).

Consolidation of the network is associated with the residual stresses that develop at the late EISA stages (*51*). This is experimentally demonstrated by the measured time-dependent deflection of a glass cantilever supporting a CNF suspension that is subjected to drying (fig. S14). From a CNF concentration of 2.5 wt %, which is nearly twice the concentration at the gelation point (figs. S12 and S13), the "frozen" water layer around the nanofibrils is overcome by capillary stresses, leading to the formation of supramolecular bonds between the fibrils and the neighboring surfaces, depending on their surface chemistry. At this stage, the surface chemistry of the rigid particles plays a dominant role in coupling fibril-fibril and fibril-particle capillary forces. Compared to hydrophilic surfaces, a lower drying stress develops for hydrophobic surfaces (*51*), which is the result of the negligible or limited interactions between the hydrophilic cellulosic surface and the hydrophobic substrate. This phenomenon explains the low conformability of the fibrils around the hydrophobized surfaces, but it gives limited insights into the overall effect of the CNF-SiO_2 system on the development of drying stresses. This determines, to some extent, the final nanostructure of the SPs. In traditional fiber physics, the strength of a fiber network correlates with the crowding factor (N) that accounts for the dimensions and volume fraction of the fibers to yield the number of fibers in a spherical volume with diameter equal to the fiber length (*52*). Therein, the number of fiber-fiber contacts is proportional to the crowding factor (N). Here, we modified the crowding factor to account for a fiber population surrounding a spherical particle, denoted as surface crowding factor (N_S). We also derived a contact crowding factor (N_C) that considers the probability of a nearby fiber to cross the particle surface (details found in section S12). Smaller particles have proportionally smaller chance for a fiber-particle encounter. Therefore, N and, more generally, N_C describe the fibril-fibril and fibril-particle interaction, respectively, as a function of concentration and particle size. Thereafter, N_S is a descriptor of fibril-fibril crowding around the particles. At the concentration range where the stresses develop in pure CNF suspensions (2.5 to 4 wt %; fig. S14), the different CNF-SiO_2 systems correspond to increasing contact crowding states for larger particles (fig. S15C). Here, we assumed N_S or $N_C < 1$ as a dilute state, $1 < N_S$ or $N_C < 100$ as a semiconcentrated state, and N_S or $N_C > 100$ as a concentrated state, based on the dimensions of the fibrils studied here (*52*). In the stress developing concentrations, due to the large length of the CNFs, the SiO_2 particles are surrounded in each case by several possible interconnections ($N_S > 50$). At the concentration when the residual stress starts developing, the contact probability is sufficiently low that the N_C is few orders of magnitude smaller than the N_S for the smallest particle size (20 nm), leading to large discrepancy between fiber-fiber and fiber-particle contacts. Around at the intermediate sizes, the suspension experiences the transition in the semi-concentrated state, which is approximately where 230 nm to 1.15 μm are optimally used, as also supported by the optimized mechanical robustness. For the largest SiO_2 particles (40 μm), the increase in volume fraction takes place only in the concentrated region, wherein the multitude of interconnection opportunities ($N_S = 10^5$ to 20^5) is also amply exploited ($N_C \approx N_S/2$). Therefore, combined with our experimental data on the mechanical strength of the CNF-based SPs, we further identified that

the peak of mechanical performance is attained when the number of fiber-particle and fiber-fiber contacts is of similar magnitude.

Topological variety and consequences on cohesion

The SPs obtained were homogeneous due to the early entrapment of the particles within the still loose but gelled nanofibrillar network. The early gelation of the CNF-particle suspensions, driven mostly by CNF (gel formation at more than 10-fold lower concentration compared to that of the suspensions of neat particles; fig. S12), prevented demixing of the two components across the SPs, without the formation of denser shells near the surface of SPs (fig. S16). SEM images of the cross-section and surface of SPs built with 20- and 230-nm SiO_2 particles show the same random particle packing interconnected with CNFs. This is also associated with the process being slow, thus reducing the early formation of a (dried) shell. Particularly for hydrophilic particles, the network formed in the gelled stage will determine the final architecture built across the SPs, regardless of the maximum packing that could be obtained as a function of particle sizes. In the interstitial spaces (for larger particles), capillary forces between the CNFs are dominant due to increased contact areas. In addition, coupling between interfibril and fibril-particle's capillary forces occurs at their interfaces (*51*). Therefore, during the latter stages of EISA, the particles accommodate within the CNF fibrillar network corresponding to the relation of their dimensions. The relationship between the relative surface area for particles and CNF (SSA ratio) drives the balance between the interfibril and fibril-particle connectivity, and therefore the mechanical performance of the final SPs.

As demonstrated in Fig. 2, the topology of the formed network strongly depends on the ratio of the dimensions of the particles and CNFs. A disconnected network is observed for particles with dimensions near the diameter of the fibrils, a sheet-like network for particles with a diameter >1000 times the fibrils' diameter, and a continuous 3D network for particles diameter 5 to 30 times the fibrils' diameter. Furthermore, as introduced in Fig. 5, the diameter alone cannot fully describe the relationship with network topology and associated cohesion. To further understand the topology of the network as a function of the particles' dimensions, we prepared multimodal particulate systems in which at least one group of particles can easily accommodate during EISA in the interstitial spaces of another particle group (e.g., 20-nm and 40-μm SiO_2 co-suspensions) (fig. S17). Therefore, the topology of the CNF network around the bigger particles is affected by the particles from the smaller group. Multimodal suspensions containing SiO_2 particles with sizes of the same order of magnitude formed SPs as strong as their single-size counterpart, regardless of the mass proportion of the individual components; however, as expected, SPs prepared from suspensions of very distinct particle sizes (20-nm/40-μm or 20-nm/230-nm particle mixtures) presented a notable lower mechanical strength (fig. S17, A and B). SEM images of SPs obtained from 1:1 mass and SSA ratio of 20- and 230-nm SiO_2 particles show a clear accumulation of colloidal particles in the interstices between the 230-nm particles (fig. S17, E and F). An equal mass ratio of particles led to a much higher number of smaller particles in the SPs, sufficient to create co-networks of CNF and smaller particles enveloping a network of bigger particles. In addition, particles in the size range tested (20 nm) are known to promote strong adhesion (*53*). However, the constructs bound only by spherical particles have a brittle character (fig. S17B) due to weak tangential contacts, with toughness much smaller than the ones bound by CNF nanofibrillar networks (Fig. 3). Reducing the number of small particles (20 nm) in the 230-nm SiO_2-CNF network led to SPs with poor mechanical performance (fig. S17B). In this case, the number of small particles is not enough to form a continuous network with the CNF around the bigger particles, leading to the formation of defects and heterogeneity in the formation of the fibril-particle network.

Scaling parameters

From the understanding of the fibril-particle network formation mechanism, we could interpret the physical meaning of our described scaling laws for CNF-induced cohesion. The proportionality constant *a*, which follows a linear log-log relation with the particle size (Fig. 3D), describes the overall contribution of the relative dimensional domain to the cohesion. The value of *a* relates to the nature of the network, in which the logarithmic relation describes a gradual conversion of a randomly oriented 3D fibrillar to a 2D network as the SiO_2 size increases. The proportionality constant can also be correlated to interfibril entanglement, where a high density of these interactions is expected in the networks, producing sheets or domains of, principally, nanocelluloses. The decay factor, *k*, that is central to the scaling law differs greatly for particle sizes with rapid Brownian motion when compared to those in the broad range between 230 nm and 40 μm. This happens because of higher density of interparticle interactions that cannot be neglected across the SP. The constant decay rate for the other hydrophilic particle sizes (230 nm to 40 μm) indicates the nature of the CNF-derived adhesion forces, ever present in the system. Our cohesion descriptor, *k*, drastically changes for SPs built with particles of different surface chemistry, e.g., cationic and hydrophobic. We attribute these differences to the changes in the particle-fibril network deriving from the variable particle-fibril interfacial interactions. The power law parameters also indicate a 2D network for $SiCH_3$ SPs and a 3D network of aggregates for the $SiNH_3^+$, as further confirmed by SEM images (fig. S6). Whereas the native SiO_2 is expected to have weak interparticle and fibril-particle interactions, driven mostly by H-bonding and van der Walls (*54*), $SiCH_3$ displays, at most, an unfavorable fibril-particle interaction but a strong interparticle attraction due to hydrophobic effects. Cationic particles interact strongly with cellulose and form ionic complexes (*55*), thus creating a stronger fibril-particle interface compared to the fibril-fibril interactions. Variations at the fibril-particle interfacial interactions correlated very well with the scaling cohesion factor, *k*, and with the fibril-particle network formation, which was described by the proportionality constant *a*. In this study, we demonstrate the viability of the approach with fibrils of six different dimensions. The relationships may be further unified into a universal scaling law for CNF-induced cohesion by using a wider scope of parameters, including surface accessibility and relative surface charge, among others.

In conclusion, we investigated a broad variety of particles to demonstrate the adhesive power of CNF to induce high cohesion in particle constructs. These constructs are readily scalable into macroscopic objects, as we briefly demonstrate by printing a 3D object (by direct ink writing) using SiO_2-CNF suspensions (Fig. 4B). The unique set of properties of CNF enables versatile and conformable fibrillar networking depending on the geometrical, dimensional, and compositional factors, as introduced by any nano- or microparticles. The noted high adhesion brought by CNF introduces a new level of mechanical robustness, applicable even in the absence

of strong particle-fibril or interparticle interactions. We quantitatively describe the scaling laws for the cohesion of the CNF-particle assemblies as a function of their relative surface areas. These scaling factors, proportional to the relative surface areas between particles and fibrils, apply to a broad range of particles sizes, from 230 nm to 40 μm. The scaling factor shifts to higher values when there is near-zero particle-fibril interactions, and to lower values when strong particle-fibril interactions take place. We highlight that an aqueous-based, CNF-centered nano-, micro-, or macrofabrication can potentially overcome all the challenges of assembling higher hierarchy particles, such as biological materials, cells and zygotes, as well as virtually any functional particle. Another interesting aspect is that physical confinement of cells by CNF networks may bring opportunities to engineer bioreactors, by allowing control over mitosis rate and mass transport of reactants and products in and out of the cells' constructs (*56*). Our results related to CNF-assisted particle assembly indicate that it is possible to overcome the restrictions imposed by packing and solvent type as well as thermal instability and differences in surface affinity between particles. Therefore, the offered advances are expected to offset existing limitations in synthesis efforts and to enable successful large-scale applications. Last, our results provide a framework to predict the scaling laws that exist for adhesion of assemblies derived from other biocolloids and fibrillar structures.

MATERIALS AND METHODS

See the Supplementary Materials for a detailed description of preparation of the CNFs, synthesis and modification of building block particles, characterizations, and isolation of the CNFs from the SPs and analytical methods.

SP assembly by EISA

All materials were assembled by EISA from aqueous suspensions. SiO_2 particles were suspended in MilliQ water at concentrations ranging from 5 to 30 wt %. The initial CNF suspension was prepared at 1.5 wt %. Both suspensions were then mixed at different proportions to achieve given particle-to-CNF ratios—with CNF solid fraction ranging from 0.3 to 15 wt % of the dried materials. The dispersions were homogenized through sequential vortexing and mild ultrasonication cycles (typically three to five). Spherical SPs were assembled by casting 5 to 20 μl of the dispersion onto a superhydrophobic surface (Teflon-coated glass slides). To avoid foaming of the dispersions of CNF and hydrophobic building blocks, a small amount of ethanol was added (<20%, v/v).

Additional particles were used to validate the scaling laws described for the CNF/SiO_2-based SPs. These particles included iron(II,III) oxide, titanium(IV) oxide, montmorillonite, halloysite, Kraft lignin, polystyrene, weed pollen, and yeast. All the SPs from non-SiO_2 particles were assembled with fixed CNF fraction (5 wt %).

SUPPLEMENTARY MATERIALS

Supplementary material for this article is available at http://advances.sciencemag.org/cgi/content/full/6/19/eaaz7328/DC1

REFERENCES AND NOTES

1. J. Guo, M. Suástegui, K. K. Sakimoto, V. M. Moody, G. Xiao, D. G. Nocera, N. S. Joshi, Light-driven fine chemical production in yeast biohybrids. *Science* **362**, 813–816 (2018).
2. J. Guo, B. L. Tardy, A. J. Christofferson, Y. Dai, J. J. Richardson, W. Zhu, M. Hu, Y. Ju, J. Cui, R. R. Dagastine, I. Yarovsky, F. Caruso, Modular assembly of superstructures from polyphenol-functionalized building blocks. *Nat. Nanotechnol.* **11**, 1105–1111 (2016).
3. K. Han, C. W. Shields IV, N. M. Diwakar, B. Bharti, G. P. López, O. D. Velev, Sequence-encoded colloidal origami and microbot assemblies from patchy magnetic cubes. *Sci. Adv.* **3**, e1701108 (2017).
4. W. B. Rogers, W. M. Shih, V. N. Manoharan, Using DNA to program the self-assembly of colloidal nanoparticles and microparticles. *Nat. Rev. Mater.* **1**, 16008 (2016).
5. S. Wintzheimer, T. Granath, M. Oppmann, T. Kister, T. Thai, T. Kraus, N. Vogel, K. Mandel, Supraparticles: Functionality from uniform structural motifs. *ACS Nano* **12**, 5093–5120 (2018).
6. M. A. Boles, M. Engel, D. V. Talapin, Self-assembly of colloidal nanocrystals: From intricate structures to functional materials. *Chem. Rev.* **116**, 11220–11289 (2016).
7. T.-S. Wei, B. Y. Ahn, J. Grotto, J. A. Lewis, 3D printing of customized li-ion batteries with thick electrodes. *Adv. Mater.* **30**, e1703027 (2018).
8. M. Sperling, H.-J. Kim, O. D. Velev, M. Gradzielski, Active steerable catalytic supraparticles shuttling on preprogrammed vertical trajectories. *Adv. Mater. Interfaces* **3**, 1600095 (2016).
9. S.-Z. Guo, K. Qiu, F. Meng, S. H. Park, M. C. McAlpine, 3D printed stretchable tactile sensors. *Adv. Mater.* **29**, 1701218 (2017).
10. C. Avci, I. Imaz, A. Carné-Sánchez, J. A. Pariente, N. Tasios, J. Pérez-Carvajal, M. I. Alonso, A. Blanco, M. Dijkstra, C. López, D. Maspoch, Self-assembly of polyhedral metal–organic framework particles into three-dimensional ordered superstructures. *Nat. Chem.* **10**, 78–84 (2017).
11. L. Y. T. Chou, K. Zagorovsky, W. C. W. Chan, DNA assembly of nanoparticle superstructures for controlled biological delivery and elimination. *Nat. Nanotechnol.* **9**, 148–155 (2014).
12. Y. Wang, A. K. Wise, J. Tan, J. W. Maina, R. K. Shepherd, F. Caruso, Mesoporous silica supraparticles for sustained inner-ear drug delivery. *Small* **10**, 4244–4248 (2014).
13. P. G. de Gennes, T. A. Witten, Scaling concepts in polymer physics. *Phys. Today* **33**, 51 (1980).
14. J. S. Oh, Y. Wang, D. J. Pine, G.-R. Yi, High-density PEO-*b*-DNA brushes on polymer particles for colloidal superstructures. *Chem. Mater.* **27**, 8337–8344 (2015).
15. M. Niederberger, H. Cölfen, Oriented attachment and mesocrystals: Non-classical crystallization mechanisms based on nanoparticle assembly. *Phys. Chem. Chem. Phys.* **8**, 3271–3287 (2006).
16. J. Lee, J. Yang, S. G. Kwon, T. Hyeon, Nonclassical nucleation and growth of inorganic nanoparticles. *Nat. Rev. Mater.* **1**, 16034 (2016).
17. J. Zhu, M. Yang, A. Emre, J. H. Bahng, L. Xu, J. Yeom, B. Yeom, Y. Kim, K. Johnson, P. Green, N. A. Kotov, Branched aramid nanofibers. *Angew. Chemie Int. Ed. Engl.* **56**, 11744–11748 (2017).
18. L. Xu, X. Zhao, C. Xu, N. A. Kotov, Water-rich biomimetic composites with abiotic self-organizing nanofiber network. *Adv. Mater.* **30**, 1703343 (2018).
19. N. Lavoine, L. Bergström, Nanocellulose-based foams and aerogels: Processing, properties, and applications. *J. Mater. Chem. A* **5**, 16105–16117 (2017).
20. B. Wicklein, A. Kocjan, G. Salazar-Alvarez, F. Carosio, G. Camino, M. Antonietti, L. Bergström, Thermally insulating and fire-retardant lightweight anisotropic foams based on nanocellulose and graphene oxide. *Nat. Nanotechnol.* **10**, 277–283 (2014).
21. R. R. Lahiji, X. Xu, R. Reifenberger, A. Raman, A. Rudie, R. J. Moon, Atomic force microscopy characterization of cellulose nanocrystals. *Langmuir* **26**, 4480–4488 (2010).
22. R. J. Moon, A. Martini, J. Nairn, J. Simonsen, J. Youngblood, Cellulose nanomaterials review: Structure, properties and nanocomposites. *Chem. Soc. Rev.* **40**, 3941–3994 (2011).
23. E. Kontturi, P. Laaksonen, M. B. Linder, Nonappa, A. H. Gröschel, O. J. Rojas, O. Ikkala, Advanced materials through assembly of nanocelluloses. *Adv. Mater.* **30**, e1703779 (2018).
24. R. T. Olsson, M. A. S. Azizi Samir, G. Salazar-Alvarez, L. Belova, V. Ström, L. A. Berglund, O. Ikkala, J. Nogués, U. W. Gedde, Making flexible magnetic aerogels and stiff magnetic nanopaper using cellulose nanofibrils as templates. *Nat. Nanotechnol.* **5**, 584–588 (2010).
25. C. Chen, L. Hu, Nanocellulose toward advanced energy storage devices: Structure and electrochemistry. *Acc. Chem. Res.* **51**, 3154–3165 (2018).
26. J.-H. Kim, D. Lee, Y.-H. Lee, W. Chen, S.-Y. Lee, Nanocellulose for energy storage systems: Beyond the limits of synthetic materials. *Adv. Mater.* **31**, 1804826 (2018).
27. N. Keshavarzi, F. Mashayekhy Rad, A. Mace, F. Ansari, F. Akhtar, U. Nilsson, L. Berglund, L. Bergström, Nanocellulose–zeolite composite films for odor elimination. *ACS Appl. Mater. Interfaces* **7**, 14254–14262 (2015).
28. M. Matsumoto, T. Kitaoka, Ultraselective gas separation by nanoporous metal–organic frameworks embedded in gas-barrier nanocellulose films. *Adv. Mater.* **28**, 1765–1769 (2016).
29. M. A. Lucchini, E. Lizundia, S. Moser, M. Niederberger, G. Nyström, Titania-cellulose hybrid monolith for in-flow purification of water under solar illumination. *ACS Appl. Mater. Interfaces* **10**, 29599–29607 (2018).
30. H. Zhu, S. Zhu, Z. Jia, S. Parvinian, Y. Li, O. Vaaland, L. Hu, T. Li, Anomalous scaling law of strength and toughness of cellulose nanopaper. *Proc. Natl. Acad. Sci.* **112**, 8971–8976 (2015).

31. Y. Habibi, L. A. Lucia, O. J. Rojas, Cellulose nanocrystals: Chemistry, self-assembly, and applications. *Chem. Rev.* **110**, 3479–3500 (2010).
32. D. J. Gardner, G. S. Oporto, R. Mills, M. A. S. A. Samir, Adhesion and surface issues in cellulose and nanocellulose. *J. Adhes. Sci. Technol.* **22**, 545–567 (2008).
33. R. Parthasarathi, G. Bellesia, S. P. S. Chundawat, B. E. Dale, P. Langan, S. Gnanakaran, Insights into hydrogen bonding and stacking interactions in cellulose. *J. Phys. Chem. A* **115**, 14191–14202 (2011).
34. N. Mittal, F. Ansari, K. Gowda V, C. Brouzet, P. Chen, P. T. Larsson, S. V. Roth, F. Lundell, L. Wågberg, N. A. Kotov, L. D. Söderberg, Multiscale control of nanocellulose assembly: Transferring remarkable nanoscale fibril mechanics to macroscale fibers. *ACS Nano* **12**, 6378–6388 (2018).
35. D. M. Kuncicky, K. Bose, K. D. Costa, O. D. Velev, Sessile droplet templating of miniature porous hemispheres from colloid crystals. *Chem. Mater.* **19**, 141–143 (2007).
36. V. Rastogi, A. A. García, M. Marquez, O. D. Velev, Anisotropic particle synthesis inside droplet templates on superhydrophobic surfaces. *Macromol. Rapid Commun.* **31**, 190–195 (2010).
37. O. D. Velev, B. G. Prevo, K. H. Bhatt, On-chip manipulation of free droplets. *Nature* **426**, 515–516 (2003).
38. O. D. Velev, A. M. Lenhoff, E. W. Kaler, A class of microstructured particles through colloidal crystallization. *Science* **287**, 2240–2243 (2000).
39. B. D. Mattos, B. L. Tardy, O. J. Rojas, Accounting for substrate interactions in the measurement of the dimensions of cellulose nanofibrils. *Biomacromolecules* **20**, 2657–2665 (2019).
40. K. J. De France, T. Hoare, E. D. Cranston, Review of hydrogels and aerogels containing nanocellulose. *Chem. Mater.* **29**, 4609–4631 (2017).
41. S. Antonyuk, J. Tomas, S. Heinrich, L. Mörl, Breakage behaviour of spherical granulates by compression. *Chem. Eng. Sci.* **60**, 4031–4044 (2005).
42. K. Livanov, L. Yang, A. Nissenbaum, H. D. Wagner, Interphase tuning for stronger and tougher composites. *Sci. Rep.* **6**, 26305 (2016).
43. P. Podsiadlo, S.-Y. Choi, B. Shim, J. Lee, M. Cuddihy, N. A. Kotov, Molecularly engineered nanocomposites: Layer-by-layer assembly of cellulose nanocrystals. *Biomacromolecules* **6**, 2914–2918 (2005).
44. H. P. S. Abdul Khalil, Y. Davoudpour, M. N. Islam, A. Mustapha, K. Sudesh, R. Dungani, M. Jawaid, Production and modification of nanofibrillated cellulose using various mechanical processes: A review. *Carbohydr. Polym.* **99**, 649–665 (2014).
45. T. Watermann, D. Sebastiani, Liquid water confined in cellulose with variable interfacial hydrophilicity. *Z. Phys. Chem.* **232**, 989–1002 (2018).
46. R. Sinko, X. Qin, S. Keten, Interfacial mechanics of cellulose nanocrystals. *MRS Bull.* **40**, 340–348 (2015).
47. H. Hatakeyama, T. Hatakeyama, Interaction between water and hydrophilic polymers. *Thermochim. Acta* **308**, 3–22 (1998).
48. C. Driemeier, F. M. Mendes, M. M. Oliveira, Dynamic vapor sorption and thermoporometry to probe water in celluloses. *Cellulose* **19**, 1051–1063 (2012).
49. Y. Peng, D. J. Gardner, Y. Han, Drying cellulose nanofibrils: In search of a suitable method. *Cellulose* **19**, 91–102 (2012).
50. S. M. Notley, B. Pettersson, L. Wågberg, Direct measurement of attractive van der waals' forces between regenerated cellulose surfaces in an aqueous environment. *J. Am. Chem. Soc.* **126**, 13930–13931 (2004).
51. B. L. Tardy, B. D. Mattos, L. G. Greca, T. Kämäräinen, K. W. Klockars, O. J. Rojas, Tessellation of chiral-nematic cellulose nanocrystal films by microtemplating. *Adv. Funct. Mater.* **29**, 1808518 (2019).
52. R. J. Kerekes, C. J. Schell, Characterization of fibre flocculation regimes by a crowding factor. *J. Pulp Pap. Sci.* **18**, 32–38 (1992).
53. S. Rose, A. Prevoteau, P. Elzière, D. Hourdet, A. Marcellan, L. Leibler, Nanoparticle solutions as adhesives for gels and biological tissues. *Nature* **505**, 382–385 (2014).
54. I. L. Radtchenko, G. Papastavrou, M. Borkovec, Direct force measurements between cellulose surfaces and colloidal silica particles. *Biomacromolecules* **6**, 3057–3066 (2005).
55. L. Wågberg, G. Decher, M. Norgren, T. Lindström, M. Ankerfors, K. Axnäs, The build-up of polyelectrolyte multilayers of microfibrillated cellulose and cationic polyelectrolytes. *Langmuir* **24**, 784–795 (2008).
56. S. H. Mohd Azhar, R. Abdulla, S. A. Jambo, H. Marbawi, J. A. Gansau, A. A. Mohd Faik, K. F. Rodrigues, Yeasts in sustainable bioethanol production: A review. *Biochem. Biophys. Rep.* **10**, 52–61 (2017).
57. T. Abitbol, A. Rivkin, Y. Cao, Y. Nevo, E. Abraham, T. Ben-Shalom, S. Lapidot, O. Shoseyov, Nanocellulose, a tiny fiber with huge applications. *Curr. Opin. Biotechnol.* **39**, 76–88 (2016).
58. I. Usov, G. Nyström, J. Adamcik, S. Handschin, C. Schütz, A. Fall, L. Bergström, R. Mezzenga, Understanding nanocellulose chirality and structure–properties relationship at the single fibril level. *Nat. Commun.* **6**, 7564 (2015).
59. Y. Zhao, C. Moser, M. E. Lindström, G. Henriksson, J. Li, Cellulose nanofibers from softwood, hardwood, and tunicate: Preparation–structure–film performance interrelation. *ACS Appl. Mater. Interfaces* **9**, 13508–13519 (2017).
60. A. Swerin, O. Lars, L. Tom, Deswelling of hardwood kraft pulp fibers by cationic polymers. *Nord. Pulp Pap. Res. J.* **5**, 188–196 (1990).
61. W. Stöber, A. Fink, E. Bohn, Controlled growth of monodisperse silica spheres in the micron size range. *J. Colloid Interface Sci.* **26**, 62–69 (1968).
62. J. H. Zhang, P. Zhan, Z. L. Wang, W. Y. Zhang, N. B. Ming, Preparation of monodisperse silica particles with controllable size and shape. *J. Mater. Res.* **18**, 649–653 (2003).
63. E. Soto-Cantu, R. Cueto, J. Koch, P. S. Russo, Synthesis and rapid characterization of amine-functionalized silica. *Langmuir* **28**, 5562–5569 (2012).
64. M. Ago, S. Huan, M. Borghei, J. Raula, E. I. Kauppinen, O. J. Rojas, High-throughput synthesis of lignin particles (~30 nm to ~2 μm) via aerosol flow reactor: Size fractionation and utilization in pickering emulsions. *ACS Appl. Mater. Interfaces* **8**, 23302–23310 (2016).
65. M. Geszke-Moritz, M. Moritz, APTES-modified mesoporous silicas as the carriers for poorly water-soluble drug. Modeling of diflunisal adsorption and release. *Appl. Surf. Sci.* **368**, 348–359 (2016).
66. D. B. Mahadik, A. V. Rao, A. P. Rao, P. B. Wagh, S. V. Ingale, S. C. Gupta, Effect of concentration of trimethylchlorosilane (TMCS) and hexamethyldisilazane (HMDZ) silylating agents on surface free energy of silica aerogels. *J. Colloid Interface Sci.* **356**, 298–302 (2011).
67. F. M. Fowkes, Additivity of intermolecular forces at interfaces. I. Determination of the contribution to surface and interfacial tensions of dispersion forces in various liquids. *J. Phys. Chem.* **67**, 2538–2541 (1963).
68. L. G. Greca, J. Lehtonen, B. L. Tardy, J. Guo, O. J. Rojas, Biofabrication of multifunctional nanocellulosic 3D structures: A facile and customizable route. *Mater. Horiz.* **5**, 408–415 (2018).
69. B. Lu, S. Torquato, Nearest-surface distribution functions for polydispersed particle systems. *Phys. Rev. A* **45**, 5530–5544 (1992).
70. I. N. Bronshtein, K. A. Semendyayev, G. Musiol, H. Mühlig, *Handbook of Mathematics* (Springer, ed. 5, 2015).

Acknowledgments

Funding: We are thankful for the funding from the ERC Advanced Grant (no. 788489, BioELCell), the Canada Excellence Research Chair initiative and the Canada Foundation for Innovation (CFI). We are also grateful for support from the Academy of Finland's Biofuture 2025 program (project 3D-Manufacturing of Novel Biomaterials 2228357-4) as well as SIRAF. W.L.E.M. is thankful to the National Council for Scientific and Technological Development (CNPq) for the fellowship of research productivity. L.G.G. acknowledges funding from the Aalto University School of Chemical Engineering doctoral programme. This work used facilities and technical support of Aalto University OtaNano–Nanomicroscopy Center (Aalto-NMC). **Author contributions:** B.D.M. conceptualized the project, synthesized and modified the particles, assembled the CNF-bound SPs, characterized the samples, analyzed the data, discussed the results, and wrote the paper. B.L.T. co-conceptualized the project, co-supervised, and wrote the paper. L.G.G. contributed with the mechanical characterization of the materials. O.C. and W.L.E.M. participated in the discussion of the results. T.K. provided the physical and morphological interpretation of CNF-driven cohesion. W.X. performed the rheology measurements. O.J.R. supervised the work and revised the paper. **Competing interests:** The authors declare that they have no competing interests. **Data and materials availability:** All data needed to evaluate the conclusions in the paper are present in the paper and/or the Supplementary Materials. Additional data related to this paper may be requested from the authors.

Submitted 4 October 2019
Accepted 24 February 2020
Published 8 May 2020
10.1126/sciadv.aaz7328

Citation: B. D. Mattos, B. L. Tardy, L. G. Greca, T. Kämäräinen, W. Xiang, O. Cusola, W. L. E. Magalhães, O. J. Rojas, Nanofibrillar networks enable universal assembly of superstructured particle constructs. *Sci. Adv.* **6**, eaaz7328 (2020).

Science Advances

Nanofibrillar networks enable universal assembly of superstructured particle constructs

B. D. Mattos, B. L. Tardy, L. G. Greca, T. Kämäräinen, W. Xiang, O. Cusola, W. L. E. Magalhães and O. J. Rojas

Sci Adv **6** (19), eaaz7328.
DOI: 10.1126/sciadv.aaz7328

Science Advances (ISSN 2375-2548) is published by the American Association for the Advancement of Science, 1200 New York Avenue NW, Washington, DC 20005. The title *Science Advances* is a registered trademark of AAAS.